IEEE Access
Multidisciplinary | Rapid Review | Open Access Journal

Received November 6, 2020, accepted November 17, 2020, date of publication November 20, 2020,
date of current version December 9, 2020.

Digital Object Identifier 10.1109/ACCESS.2020.3039505

Dual Quasi-Resonant Controller Position Observer Based on High Frequency Pulse Voltage Injection Method

YI MAO, YI DU, (Member, IEEE), ZHUOFAN HE, LI QUAN, XIAOYONG ZHU, (Member, IEEE), LI ZHANG, (Member, IEEE), AND YUEFEI ZUO, (Member, IEEE)
School of Electrical and Information Engineering, Jiangsu University, Zhenjiang 212013, China

Corresponding author: Yi Du (duyie@ujs.edu.cn)

This work was supported in part by the National Natural Science Foundation of China under Grant 51677081, Grant 51877099, and Grant 51777089; in part by the Qinglan Project of Jiangsu Province; and in part by the Priority Academic Program Development of Jiangsu Higher Education Institutions.

ABSTRACT This paper proposed a dual quasi-resonant controller position observer for conventional pulsating high frequency voltage injection method. The proposed position observer can not only improve the dynamic performance of the sensorless control, but can also compensate the position error fluctuation caused by the dead-time effect. To improve the dynamic performance, the digital bandpass filter in the traditional position observer used to extract high frequency current response is replaced by a quasi-resonant controller firstly. Moreover, an improved Luenberger observer without lowpass filter, which is usually used in traditional position observer to filter the noise in speed information, is adopted in the new position observer. Therefore, dynamic performances can be improved. Then, to reduce the sixth harmonic in the magnitude of position error and speed error caused by the dead-time effect, a frequency adaptive quasi-resonant controller is connected in parallel with the proportional-integral controller in the Luenberger observer. The experiment results verify that the proposed observer can reduce the position estimation error not only in steady state operation conditions, but in variable speed and variable load conditions, and the speed variation range can be widened as well.

INDEX TERMS Dynamic performance improvement, position error fluctuation reduction, pulsating high frequency voltage injection method, quasi-resonant controller, sensorless control.

I. INTRODUCTION

Permanent magnet synchronous machines (PMSMs) are widely applied due to their high torque density, power density, and efficiency. To improve the output performance, a high-resolution vector control strategy that depends on the accuracy of the rotor position information should be implemented on the controller of a PMSM. Normally, the rotor position is obtained by mechanical sensors which will bring several disadvantages such as extra cost, axial size, low reliability, and noise immunity. Therefore, a large number of publications have been focused on the rotor position estimation to achieve sensorless control [1]–[5].

The associate editor coordinating the review of this manuscript and approving it for publication was Shihong Ding.

The position sensorless estimation techniques for PMSM drives can be divided into two main categories: the methods based on back electromotive force (EMF) and high-frequency signal injection [6]–[8]. For medium- to high-speed operations, back EMF-based methods have been well founded and exhibited satisfying performance. However, the rotor position cannot be extracted effectively in zero- to low-speed operations since the amplitude of back EMF signal becomes too weak to be detected precisely [9], [10].

To realize sensorless control in low speed range of PMSM, high-frequency signal injection (HFI) method is commonly used. There are two more commonly used HFI methods: rotating signal injection and pulsating signal injection [11], [12]. The former was proposed first, but it only works for machines with salient pole, means that it cannot be used

for SPMSM. As a result, the latter was proposed. It constructs a saliency for SPMSM based on the principle that the d-axis inductance will be reduced when the magnetic circuit in the d-axis is saturated. Two forms of injection scheme are compared in [13], [14]. Compared with the rotating signal injection method, the pulsating signal injection method is less sensitive to the parameter variation, more accurate and more adaptive for various kinds of machine [13], thus is more widely used.

Though the pulsating signal injection method possesses its own advantages, it is now subjected to two problems. The first is that the HF current is extracted by a constant bandwidth BPF, and a LPF is necessary to filter the noise in speed information, which will cause phase lag and decrease the dynamic performance, and this is not the best for wider speed range. [15], [16]. Mostly, the dead-time effect, which will cause the position error fluctuation in both the position error and the speed error [17], [18] is tackled as a problem in pulsating signal injection method as well.

To overcome the first drawback, an improved position observer based on square-wave voltage injection which omits the low-pass filter used to filter the noise in the speed estimation process was introduced in [19]. In [20], a simple algorithm based on square-wave voltage injection was proposed. It utilized the difference and average value of two consecutive sampling currents to figure out the high frequency current and fundamental current, so that the LPF and BPF can be removed. To cope with the position error fluctuation, numerical studies have been done. In [21], the second harmonic position error caused by parameter asymmetry in rotating or pulsating signal injection was analyzed, and a novel online strategy with dual-frequency injection was proposed to compensate the harmonic position error caused by inductance asymmetry. In [22], the position error caused by cross-saturation, which can result in sixth harmonic component in the inductances in field oriented coordinates, was analyzed. However, for the pulsating HF voltage injection method, few of them take the harmonic in the position error fluctuation caused by dead-time effect and dynamic performance into consideration at the same time.

Consequently, to compensate the position error caused by dead-time effect and improve the dynamic performance of the conventional pulsating HF voltage injection method, an improved position observer for conventional pulsating HF voltage injection method with position error compensation and fewer digital filters is designed in this paper.

In this paper, the harmonic component in position error caused by dead-time effect is analyzed firstly. Then, based on the theoretical analysis on quasi-resonant controller, an improved position observer for HF pulse voltage signal injection is proposed. In this observer, the digital BPF used to extract high frequency current response is replaced by a quasi-resonant controller, and an improved Luenberger observer is introduced to omitted the LPF used to filter the noise in speed information by using the predictive speed for the speed loop feedback. Therefore, the dynamic performance can be improved because of the reduction in the number of digital filters. Besides, to reduce the sixth harmonic in the magnitude of position error and speed error caused by dead-time effect, a PIR controller which connects a frequency adaptive quasi-resonant controller in parallel with the PI regulator in the Luenberger observer, is adopted. Finally, the effectiveness of the improved position observer is verified by experimental results on a 1.5-kW IPMSM drive platform.

II. ANALYSIS OF CONVENTIONAL PULSATING SINUSOIDAL VOLTAGE INJECTION METHOD

A. PRINCIPLE OF CONVENTIONAL PULSATING SINUSOIDAL VOLTAGE INJECTION METHOD

The schematic diagram of the conventional high-frequency pulsating sinusoidal voltage injection method [13] is shown in Fig. 1. Firstly, a HF pulsating sinusoidal voltage signal is injected into the estimated d axis to induce HF current. Then the position can be estimated through the minimization of the amplitude-modulated carrier current response that is measured along the axis which is orthogonal to the injection axis.

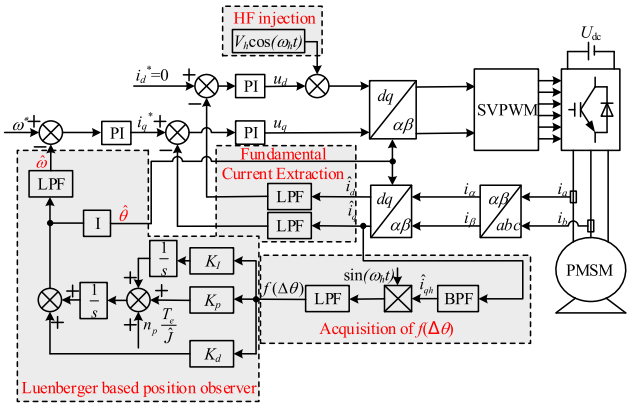

FIGURE 1. Schematic diagram of the conventional high-frequency pulsating voltage injection method.

The HF model of PMSM represented in the rotor dq axis can be modelled as (1), where the cross-saturation effects are neglected.

$$\begin{bmatrix} u_{dh} \\ u_{qh} \end{bmatrix} = \begin{bmatrix} R_s + \mathrm{j}\omega_h L_{dh} & -\omega_e L_{qh} \\ \omega_e L_{dh} & R_s + \mathrm{j}\omega_h L_{qh} \end{bmatrix} \begin{bmatrix} i_{dh} \\ i_{qh} \end{bmatrix} + \begin{bmatrix} 0 \\ \omega_e \psi_f \end{bmatrix} \tag{1}$$

where u_{dh} and u_{qh} are the HF voltage of the actual dq-axis, respectively. i_{dh} and i_{qh} are the HF current of the actual dq-axis, L_{dh} and L_{qh} are the stator HF inductances, R_s is the stator resistance, ω_e is the electrical rotor speed, ω_h is the injected HF signal, and ψ_f is the magnetic linkage flux.

If the motor operates at low speed and the injection frequency is set high enough, the voltage drops on the stator resistance and the items associated with the rotor speed in (1) can be neglected. Then, PMSM can be approximated to an

inductive load and (1) can be simplified as

$$\begin{bmatrix} u_{dh} \\ u_{qh} \end{bmatrix} = \begin{bmatrix} \mathrm{j}\omega_h L_{dh} & 0 \\ 0 & \mathrm{j}\omega_h L_{qh} \end{bmatrix} \begin{bmatrix} i_{dh} \\ i_{qh} \end{bmatrix} \tag{2}$$

If the actual rotor position is defined as θ and the estimated rotor position is $\hat{\theta}$, the difference between them is position error $\Delta\theta$. Then, the HF-induced current in the estimated synchronous reference frame can be deduced as

$$\begin{aligned} \begin{bmatrix} \hat{i}_{dh} \\ \hat{i}_{qh} \end{bmatrix} &= \frac{1}{L^2 - \Delta L^2} \\ &\times \begin{bmatrix} L - \Delta L\cos(2\Delta\theta) & -\Delta L\sin(2\Delta\theta) \\ -\Delta L\sin(2\Delta\theta) & L + \Delta L\cos(2\Delta\theta) \end{bmatrix} \\ &\times \begin{bmatrix} \hat{u}_{dh} \\ \hat{u}_{qh} \end{bmatrix} \end{aligned} \tag{3}$$

where L and $\Delta L$are the average inductance and the difference inductance respectively, and $L = (L_{dh}+L_{qh})/2$, $\Delta L = (L_{dh}-L_{qh})/2$.

When the HF voltage signal $U_h\cos(\omega_h t)$ is injected into the estimated d –axis, (3) can be obtained as

$$\begin{bmatrix} \hat{i}_{dh} \\ \hat{i}_{qh} \end{bmatrix} = \frac{U_h\sin(\omega_h t)}{L_{dh}L_{qh}\omega_h} \begin{bmatrix} L - \Delta L\cos(2\Delta\theta) \\ -\Delta L\sin(2\Delta\theta) \end{bmatrix} \tag{4}$$

It can be seen from (4) that the HF current response of the estimated q-axis, which can be extracted by a BPF, contains the relevant information of the rotor position. Then multiply the HF signal with the modulation signal $\sin(\omega_h t)$. Then the required regulator input $f(\Delta\theta)$ which contains position error information can be obtained by a LPF to filter the low frequency components

$$\begin{aligned} f(\Delta\theta) &= \mathrm{LPF}(\mathrm{BPF}(\hat{i}_q)\sin(\omega_h t)) \\ &= \frac{K}{2}\sin(2\Delta\theta) \approx K\,\Delta\theta \end{aligned} \tag{5}$$

where $K = -\frac{\Delta L U_h}{\omega_h L_{dh} L_{qh}}$.

It can be seen from (5) that if $f(\Delta\theta)$ is passed through a phase-locked loop (PLL) or an observer, the estimated position can converged with the actual position when the parameters are appropriate. Then, the position and speed information can be observed. In Fig. 1, a Luenberger observer is selected [15], [19].

B. ANALYSIS OF POSITION ERROR CAUSED BY DEAD-TIME EFFECT

In a pulse width modulation (PWM) inverter-fed PMSM drive, a dead time should be inserted in the IGBT drive signal to prevent short circuit in DC link caused by the simultaneous conduction of both switches in one inverter leg. However, such a blanking time causes serious distortion in output voltages, and then, the harmonics will occur in phase current

Assuming t_{on} is the turn-on time delay of the switching device, t_{off} is the turn-off time delay of the switching device, t_d is the dead time. Then the inverter time error T_{err} can be expressed as

$$T_{err} = t_d + t_{on} - t_{off} \tag{6}$$

Subsequently, the phase voltage error can be given as

$$U_{err} = \frac{T_{err}}{T} U_{dc} sign(i_p) \tag{7}$$

where T is the PWM carrier period, $sign(i_p)$ is a sign function of phase current, U_{dc} is the DC-link voltage.

In (7), the phase voltage error is a constant value. Therefore, the harmonic content in phase current will increase further when the motor is operating at low speed and light load. The main harmonic component superposed in the fundamental amplitude of phase current caused by dead-time is sixth harmonic [23]. Hence, the phase current can be expressed as

$$i_x = [I_1 + I_6\sin(6\omega_e t + \varphi_6)]\sin(\omega_e t + \varphi_1 + i\frac{2\pi}{3}) \tag{8}$$

where x is three phase a, b and c, respectively. i corresponds to 0, -1 and 1, respectively. ω_e is the electrical rotor speed. I_1 and φ_1 are fundamental wave amplitude and initial phase, respectively. I_6 and φ_6 are the amplitude and initial phase of sixth harmonic which is superposed in the fundamental amplitude of phase current.

By further calculating (8) with trigonometric function formula, the fifth and seventh harmonics of fundamental component in phase current can be obtained as

$$\begin{aligned} i_x &= I_1\sin(\omega_e t + \varphi_1 + i\frac{2\pi}{3}) \\ &\quad - \frac{I_6}{2}\cos(-5\omega_e t - \varphi_6 + \varphi_1 + i\frac{2\pi}{3}) \\ &\quad + \frac{I_6}{2}\cos(7\omega_e t + \varphi_6 + \varphi_1 + i\frac{2\pi}{3}) \end{aligned} \tag{9}$$

Transform (9) to SRF, therefore, the current can be expressed as

$$\begin{cases} i_d = I_1\sin\varphi_1 - I_6\sin(6\omega_e t + \varphi_6)\sin\varphi_1 \\ i_q = -I_1\cos\varphi_1 + I_6\sin(6\omega_e t + \varphi_6)\cos\varphi_1 \end{cases} \tag{10}$$

It can be simplified as

$$\begin{cases} i_d = I_d + I_{d6}\sin(6\omega_e t + \varphi_{d6}) \\ i_q = I_q + I_{q6}\sin(6\omega_e t + \varphi_{q6}) \end{cases} \tag{11}$$

where $I_d = I_1\sin\varphi_1$, $I_q = -I_1\cos\varphi_1$, $I_{d6} = -I_6\sin\varphi_1$, $I_{q6} = I_6\cos\varphi_1$, $\varphi_{d6} = \varphi_{q6} = \varphi_6$.

It can be seen from (11) that dead-time effect results in sixth harmonics in SRF. Therefore, dead-time effect will cause the sixth harmonic to be superimposed on the fundamental amplitude of the HF current in SRF [24].

$$\begin{cases} i_{dh} = [I_{dh} + I_{dh6}\sin(6\omega_e t + \varphi_{dh6})]\cdot\sin(\omega_h t + \varphi_{dh}) \\ \quad = D_h\sin(\omega_h t + \varphi_{dh}) \\ i_{qh} = [I_{qh} + I_{qh6}\sin(6\omega_e t + \varphi_{qh6})]\cdot\sin(\omega_h t + \varphi_{qh}) \\ \quad = Q_h\cdot\sin(\omega_h t + \varphi_{qh}) \end{cases} \tag{12}$$

where I_{xh} and φ_{xh} are the amplitude and initial phase of the high-frequency current, respectively. I_{xh6} and φ_{xh6} are

the amplitude and initial phase of the sixth harmonic superimposed on the amplitude of the HF current, respectively. x denotes d, q respectively. And $D_h = I_{dh} + I_{dh6}\sin(6\omega_e t + \varphi_{\mathrm{dh6}})$, $Q_h = I_{qh} + I_{qh}6\sin(6\omega_e t + \varphi_{qh6})$.

Transforming the high frequency current response of the actual dq axis in (12) to the estimated dq axis.

$$\begin{cases} \hat{i}_{dh} = (D_h\cos\Delta\theta\cos\varphi_{dh} - Q_h\sin\Delta\theta\cos\varphi_{qh})\sin(\omega_h t) \\ \qquad + (D_h\cos\Delta\theta\sin\varphi_{dh} - Q_h\sin\Delta\theta\sin\varphi_{qh})\cos(\omega_h t) \\ \hat{i}_{qh} = (D_h\sin\Delta\theta\cos\varphi_{dh} + Q_h\cos\Delta\theta\cos\varphi_{qh})\sin(\omega_h t) \\ \qquad + (D_h\sin\Delta\theta\sin\varphi_{dh} + Q_h\cos\Delta\theta\sin\varphi_{qh})\cos(\omega_h t) \end{cases} \tag{13}$$

Subsequently, the estimated q axis HF current response with the sixth harmonic component superimposed on the amplitude of the current is finally demodulated by the signal to obtain $f(\Delta\theta)$

$$\begin{aligned} f(\Delta\theta) &= \mathrm{LPF}(2\sin(\omega_h t)\cdot\hat{i}_{qh}) \\ &= D_h\sin\Delta\theta\cos\varphi_{dh} + Q_h\cos\Delta\theta\cos\varphi_{qh} \end{aligned} \tag{14}$$

It can be seen from (14) that in $f(\Delta\theta)$, besides the DC component, the sixth harmonic component of the fundamental wave is superimposed. If the estimated rotor position converges to the actual rotor position in this case, $\Delta\theta$ can be expressed as

$$\Delta\theta = -\arctan\frac{[I_{qh} + I_{qh6}\sin(6\omega_e t + \varphi_{qh6})]\cos\varphi_{qh}}{[I_{dh} + I_{dh6}\sin(6\omega_e t + \varphi_{dh6})]\cos\varphi_{dh}} \tag{15}$$

If the sixth harmonic signal in $f(\Delta\theta)$ is not processed, the sixth harmonic component of the fundamental wave will be present in the final rotor position error.

III. REVIEW OF THE QUASI-RESONANT CONTROLLER

In recent years, the Quasi-Resonant Controller has been widely used to supress multiple harmonics at resonant frequencies because of its flexibility, computation efficiency, and infinite gain of resonant controllers at resonant frequencies [25]–[27]. The transfer function of ideal resonant controller [25] can be expressed as

$$G_R(s) = \frac{2k_{ir}s}{s^2 + \omega_0^2} \tag{16}$$

where k_{ir} is the resonant coefficient, ω_0 is the resonant frequency.

For the ideal resonant controller, the gain at the resonant frequency is expressed in (17). It can be seen that the gain of $G_R(s)$ at the resonant frequency ω_0 is infinite, therefore, the steady tracking error of the frequency ω_0 in the AC reference signal can be eliminated, and the influences of the external disturbance can be completely resisted.

$$|G_R(s)|_{s=\mathrm{j}\omega_0} = \sqrt{\left(\frac{2k_{ir}\omega_0}{-(\omega_0)^2 + \omega_0^2}\right)^2} \to +\infty \tag{17}$$

However, since the gain of the resonant controller is infinite only at the resonant frequency, and the gain outside the resonant frequency decreases dramatically, which will cause the ideal resonant controller to be sensitive to the changes in the reference signal frequency, resulting in the system to fluctuate easily. Moreover, the ideal resonant controller is not conducive in practice due to its narrow bandwidth and the limitations in the precisions of the digital system. Hence, this paper adopts the quasi-resonant controller [23], [24], the transfer function can be expressed as

$$G_R(s) = \frac{2k_{ir}\omega_c s}{s^2 + 2\omega_c s + \omega_0^2} \tag{18}$$

where ω_c is the cutoff frequency of the quasi-resonant controller.

Fig. 3 represents the Bode diagram which shows the effect of parameters ω_c and k_{ir} on the performance of the quasi-resonant controller. Fig. 3(a) is the Bode diagram with k_{ir} constant at 1, ω_c changes when $\omega_0 = 1000\pi (f = 500\mathrm{HZ})$. Fig. 3(b) is the Bode diagram with ω_c constant at 250 π, k_{ir} changes when $\omega_0 = 1000\pi (f = 500\mathrm{HZ})$. Fig. 3(a) exhibits that the gain and phase of the controller at the resonant frequency point do not change, only the bandwidth of the controller changes with the change of ω_c. The bandwidth of the controller increases with the increase of ω_c, nevertheless, the excessive bandwidth will affect the frequency selection characteristics of the controller, and the speed of the system response will be affected when the bandwidth is too small. Fig. 3(b) shows that the gain of the quasi-resonant controller is proportional to k_{ir}, and large k_{ir} leads to large peak gain, but the phase and bandwidth is fixed. It also can be seen that $G_R(s)$ provides a high open-loop gain at ω_0. Therefore, the quasi-resonant controller can suppress harmonics and has an excellent tracking for the input when used in closed loop. Subsequently, the quasi-resonant controller is used to extract high frequency current response and reduce the sixth harmonic in the magnitude of position error and speed error caused by dead-time effect.

Subsequently, the equivalent principle block diagram of the quasi-resonant controller can be obtained as shown in Fig. 2.

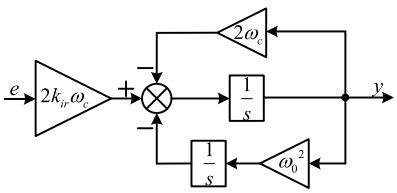

FIGURE 2. Equivalent schematic block diagram of quasi-resonant controller.

IV. DESIGN AND ANALYSIS OF IMPROVED ROTOR POSITION OBSERVER BASED ON QUASI-RESONANT CONTROLLER

Due to the effects of digital filter and dead-time effect, conventional pulsating sinusoidal voltage injection method suffers from chattering. Therefore, in this paper, an improved rotor position observer based on quasi-resonant controller is

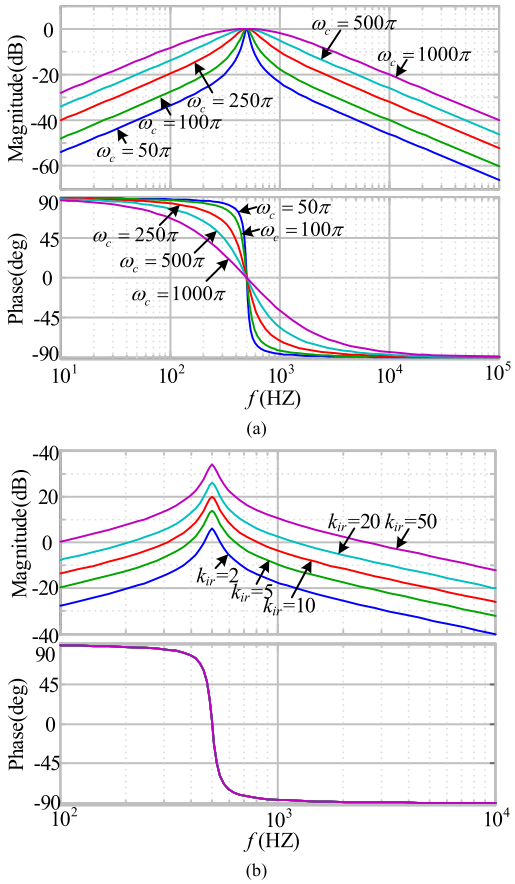

FIGURE 3. Bode diagram of the quasi-resonant controller with parameters varying. (a) ω_c. (b) k_{ir}.

proposed to improve the sensorless performance. The structure of the improved position observer is shown in Fig. 4. It includes HF current extraction module, Luenberger based position observer without LPF module and position error compensation module.

A. HF CURRENT EXTRACTION MODULE DESIGN

BPF is used to extract high frequency current response in conventional pulsating sinusoidal voltage injection method. For digital control systems, the BPF is generally implemented in the form of a digital filter. However, the tuning of the parameters is cumbersome, and the introduction of BPF will limit the bandwidth of position observers. Additionally, if the low-order BPF is selected, the required high-frequency current component cannot be effectively extracted, the signal-to-noise ratio (SNR) of the high-frequency signal is reduced, and the rotor position estimation will fluctuate greatly. While high-order BPF will introduce serious delay problem, which will affect the dynamic performance of sensorless control.

As shown in the "HF current extraction module" in Fig. 4, the BPF is replaced by a quasi-resonant controller. When the k_{ir} is constant to 1, the resonant frequency is set as the frequency of the injected signal, therefore, the adjustment of the filter characteristic can be realized by adjusting ω_c. This improvement can reduce the workload in the debugging process and the phase delay caused by the digital filter.

In addition, since the conventional BPF does not have inner loop adjustment, the HF disturbance generated by the step input cannot be effectively suppressed. Nevertheless, for the quasi-resonant controller, an inner-loop regulation exists. When the step signal is input, the output signal is quickly tracked by the signal y_1 obtained by integral feedback, thereby reducing the influence of the step input on y_2.

B. LUENBERGER BASED POSITION OBSERVER WITHOUT LPF MODULE DESIGN

For the traditional PI observer based on PLL or Luenberger observer with electromagnetic torque feedforward, the observed speed information will contain certain noise. To make the observed speed can be used for normal speed closed-loop, it is necessary to add a LPF after the observed speed to filter out the noise. However, the introduction of the LPF will greatly reduce the bandwidth of the speed loop and affect the dynamic performance of the system.

As shown in the "Luenberger based position observer without LPF module" in Fig. 4, a modified Luenberger observer is used to observe the speed. The predictive speed is used to replace the speed after the LPF. So that the LPF used to filter out the noise can be omitted, which will improve the dynamic performance of the system.

When the viscous friction is neglected, the mechanical model of the motor can be expressed as [28]

$$p\begin{bmatrix}\omega_e\\ \theta_e\end{bmatrix}=\begin{bmatrix}0 & 0\\ 1 & 0\end{bmatrix}\begin{bmatrix}\omega_e\\ \theta_e\end{bmatrix}+\begin{bmatrix}\frac{n_p}{J}T_e\\ 0\end{bmatrix}-\begin{bmatrix}\frac{n_p}{J}T_l\\ 0\end{bmatrix} \tag{19}$$

where p is the differential operator, ω_e and θ_e are the rotor electrical speed and electrical angle, T_e and T_l are the electromagnetic torque and load torque, J is the moment of inertia, n_p is the pole pair number.

In (19), the electromagnetic torque can be expressed as

$$T_e=\frac{3}{2}n_p\psi_f i_q \tag{20}$$

where ψ_f is the permanent magnet flux linkage.

Then the estimated states can be expressed as

$$p\begin{bmatrix}\hat{\omega}_e\\ \hat{\theta}_e\end{bmatrix}=\begin{bmatrix}0 & 0\\ 1 & 0\end{bmatrix}\begin{bmatrix}\hat{\omega}_e\\ \hat{\theta}_e\end{bmatrix}+\begin{bmatrix}\frac{n_p}{J}T_e\\ 0\end{bmatrix}-\begin{bmatrix}K_{pi} & 0\\ K_d & 0\end{bmatrix}\times\begin{bmatrix}\theta_e-\hat{\theta}_e\\ 0\end{bmatrix} \tag{21}$$

Through (20) (21), by selecting the observer gains K_{pi} as proportional and integral (PI) gains and K_d as a proportional gain, the "Luenberger based position observer without LPF module" in Fig. 4 can be built.

The closed-loop transfer function of Luenberger observer can be expressed as

$$\frac{\hat{\theta}_e}{\theta_e}=\frac{Js^3+Jk_ds^2+k_ps+k_i}{\hat{J}s^3+\hat{J}k_ds^2+k_ps+k_i} \tag{22}$$

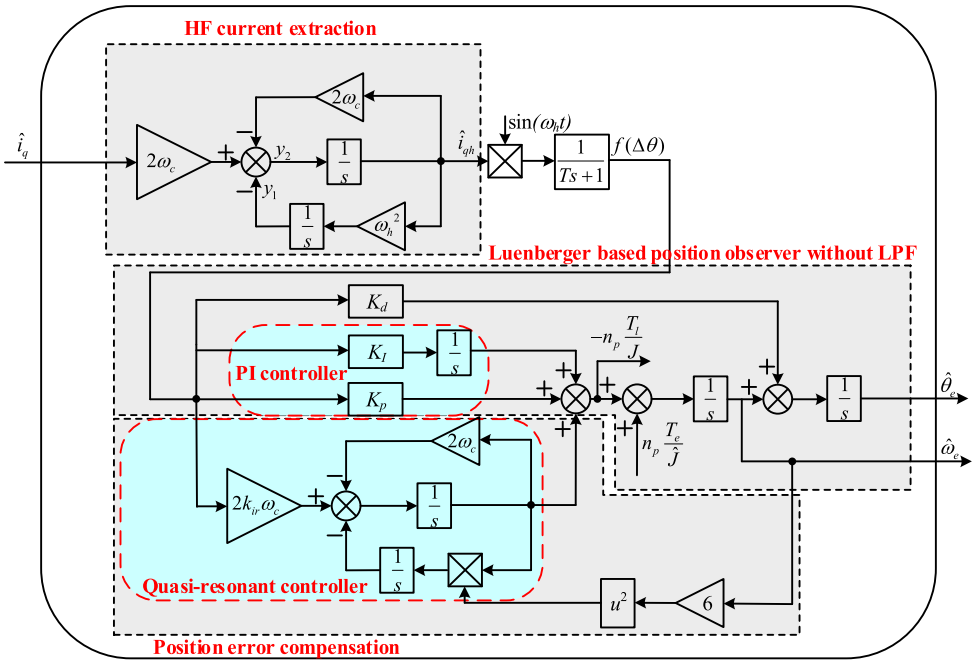

FIGURE 4. Structure of improved position observer.

where J and $\hat{J}$ are the moment of inertia and its observation, respectively, k_p, k_i and k_d are the proportional, integral, differential gain of the Luenberger observer, respectively.

Finally, the modified Luenberger observer can not only accurately identify the rotor position without phase lag, but also omits the speed LPF and improves the dynamic performance of the system.

C. POSITION ERROR COMPENSATION MODULE DESIGN BASED ON FREQUENCY ADAPTIVE QUASI-RESONANT CONTROLLER

According to the analysis in the second section, the position error information $f(\Delta\theta)$ contains the sixth harmonic component of the fundamental wave due to the dead-time effect. Then the position information is observed from $f(\Delta\theta)$ through the Luenberger observer.

A Luenberger observer is composed of three parts: PI regulator, PMSM mechanical system mathematical model and error feedforward compensation. Specifically, $f(\Delta\theta)$ outputs the signal $-n_pT_l/J$ required by the later mechanical mathematical mode through PI regulator, then calculates the speed information through the mathematical model of the motor. Finally, the stability of the system will be enhanced by error feedforward compensation.

However, the traditional PI controller can only control the DC signal without static error. When the input signal $f(\Delta\theta)$ contains AC component, the PI controller cannot compensate it, which will eventually lead to the sixth harmonic component of the fundamental wave in the rotor position error. Therefore, for the choice of the controller, it is not only required to adjust the DC component, but also to suppress the AC disturbance component.

In this paper, a proportional-integral- resonant (PIR) controller, which connects a quasi-resonant controller in parallel with the PI regulator, is adopted. The block diagram of the PIR controller scheme is shown in Fig. 5.

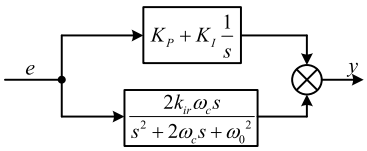

FIGURE 5. Block diagram of the PIR control scheme.

The transfer function of the PIR controller can be expressed as

$$G_{PIR}(s) = K_p + K_I\frac{1}{s} + \frac{2k_{ir}\omega_c s}{s^2 + 2\omega_c s + \omega_0^2} \tag{23}$$

Fig. 6 represents the Bode diagram of the PIR controller when $\omega_0 = 300$, $K_P = 10$, $K_I = 1$, $k_{ir} = 10$, $\omega_c = 30$. It can be seen that the open-loop gain of the controller at the resonance frequency point increases sharply, which means the controller can suppress the AC signal at the resonance frequency point well.

Therefore, to suppress the sixth harmonic component in $f(\Delta\theta)$ on the position error, the "position error compensation module" as shown in Fig. 4, which adopts a PIR controller, is proposed in this paper. Since the quasi-resonant controller can achieve zero static error control of the sinusoidal signal at the resonant frequency point, therefore, a frequency adaptive

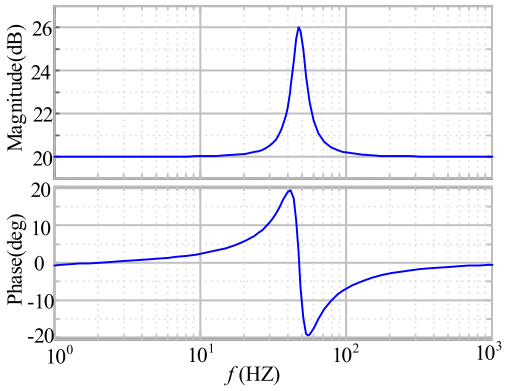

FIGURE 6. Bode diagram of the PIR controller.

quasi-resonant controller with a resonant frequency of $6\omega_e$ is connected in parallel with the PI regulator of the Luenberger observer, and ω_e adopts the observed speed. Thus, the resonant frequency of the quasi-resonant controller can be adaptively changed with the change of the angular frequency of the motor to achieve a more accurate rotor position estimation.

Finally, the improved position observer with a Luenberger observer and a quasi-resonant controller can be seen as a PIDR observer, which can accurately identify the rotor position without phase lag and reduce the influence of dead-time effect on position estimation simultaneously.

V. EXPERIMENTAL VALIDATION

To verify the validity of theoretical analysis of the proposed control method, the proposed algorithm adopted for a IPMSM, a dSPACE 1103 controller is used to drive the prototype. The experiment platform is shown in Fig. 7, which includes IPMSM for research in this paper, its parameters are shown in Table 1. The magnetic powder brake is used as a load. The actual rotor position is obtained by an incremental encoder with 1024 pulses/revolution for comparison with the observed rotor position. The switching frequency and

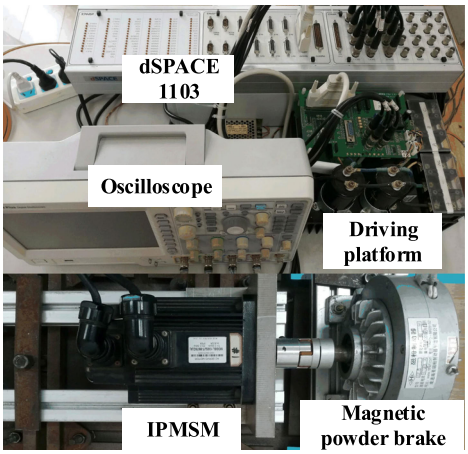

FIGURE 7. Experiment platform.

TABLE 1. Parameters of the IPMSM.

Parameters	Values	Parameters	Values
Rated voltage (V)	220	Torque constant ((N·m)/A)	0.876
Rated power (kW)	1.5	Stator resistance (Ω)	0.655
Rated speed (r/min)	2000	d-axis inductance (mH)	3.506
Number of rotor pole-pairs	4	q- axis inductance (mH)	5.793
Rated torque(N·m)	7.7	Moment of inertia(g·m^2)	1.5

deadtime of the voltage source inverters are set at 10kHz and 2μs, the current sampling frequency is 10 kHz, the DC bus voltage is 100 V.

For the proposed position observer, to obtain the position information effectively, the magnitude and frequency of the injected carrier voltage is set as 14.5V and 500Hz. ω_h of the quasi-resonant controller in the front stage is taken 1000π, because the frequency of the injected carrier voltage is 500Hz. ω_c is 500π according to the bode diagram of the quasi-resonant controller. To extract the effective component and avoid introducing serious phase lag, the parameter T of the LPF used to demodulate $f(\Delta\theta)$ is selected to be $1/(900\pi)$. The k_p, k_i and k_d of the Luenberger observer is 2.25, 30 and 100, and the parameter $\hat{J}$ is 0.0015. k_{ir} and ω_c of the quasi-resonant controller to suppress the rotor position error in the latter stage is taken as 5 and 200 according to the bode diagram of the quasi-resonant controller. The second-order Butterworth bandpass filter is selected for the traditional position observer used for comparison and the passband is set to [450HZ,550HZ].

A. EXPERIMENT RESULTS OF NO-LOAD STEADY STATE

Fig. 8 shows the comparison experimental results before and after the improved algorithm is enabled when $n = 50$rpm (2% rated speed) in no load condition. Fig. 8(a) shows the actual speed, estimated speed and speed error before and after the improved algorithm is enabled when the dead time is 2μs. Fig. 8(b) shows the actual rotor position, estimated rotor position and position error before and after the improved algorithm is enabled when the dead time is 2μs. Fig. 8(c) shows actual rotor position, estimated rotor position, speed error and position error before and after the improved algorithm is enabled when the dead time is 5μs.

From Fig. 8, it can be seen that under different dead times, the improved algorithm can effectively suppress the speed error and the rotor position error, and the fluctuation of the actual speed can be reduced at the same time, so that the motor can run more smoothly. Through the FFT analysis of the speed error and the rotor position error it is found that, when the dead time is 2μs and the improved algorithm is disabled, the amplitude of the harmonics in the speed error and the rotor position error is 4.02rpm, 5.7°. When the improved algorithm is enabled, the amplitude of the harmonics in the speed error and the rotor position error is 1.57rpm, 1.49°. Hence, compared with the traditional algorithm, the improved

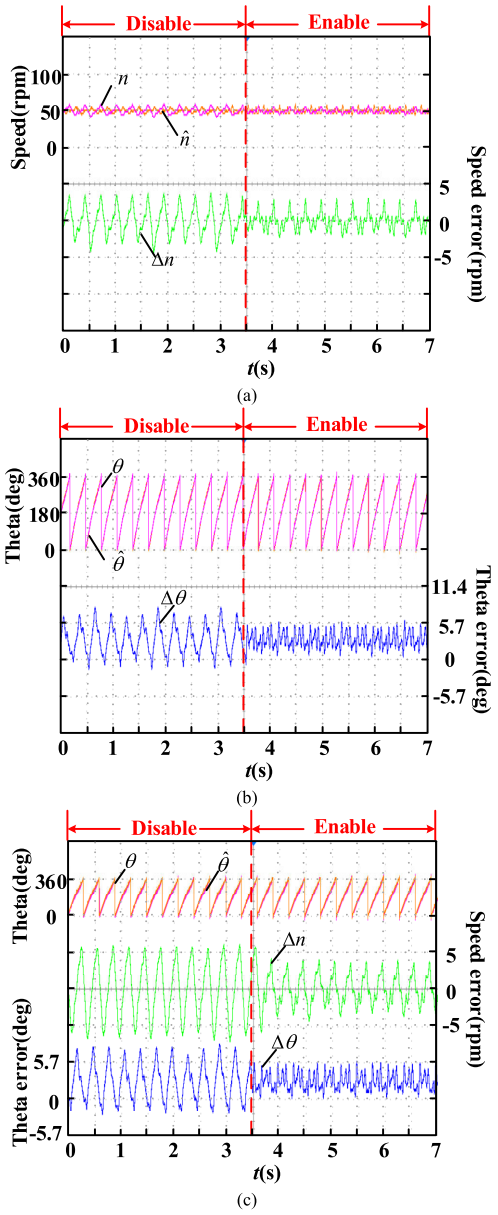

FIGURE 8. Experimental comparison with and without improved algorithm at 50rpm. (a) dead time is 2μs. (b)dead time is 2μs. (c) dead time is 5μs.

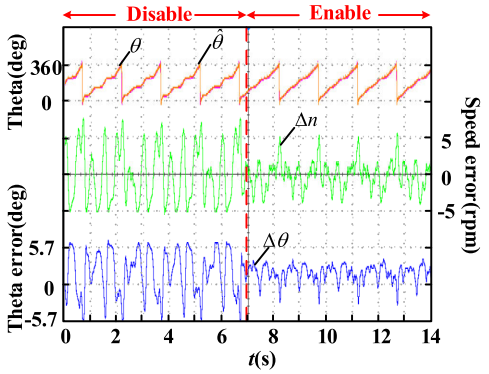

FIGURE 9. Experimental comparison with and without improved algorithm at 10rpm(dead time is 2μs).

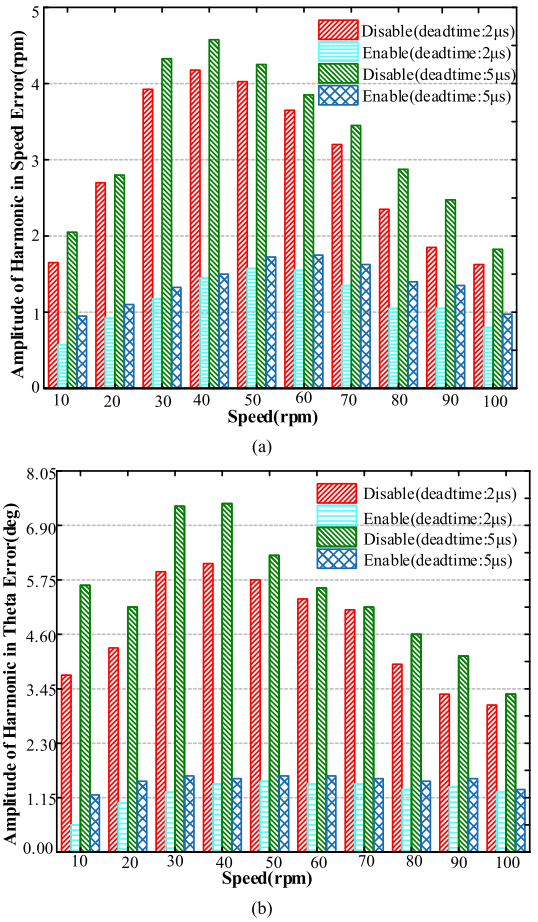

FIGURE 10. Compensation effect of the 6th harmonic. (a) speed error. (b) theta error.

algorithm improves the speed estimation accuracy by 60.9% and the rotor position estimation accuracy by 74%. Moreover, when the dead time is 5μs and the improved algorithm is disabled, the amplitude of the harmonics in the speed error and the rotor position error is 4.25rpm, 6.24°. When the improved algorithm is enabled, the amplitude of the harmonics in the speed error and the rotor position error is 1.725rpm, 1.6°, the improved algorithm improves the speed estimation accuracy by 59.4% and the rotor position estimation accuracy by 74.3%. Therefore, the improved method has good effect in different dead time.

Fig.9 shows the comparison experimental results before and after the improved algorithm is enabled when the motor is close to standstill (n = 10rpm). It can be seen that the improved algorithm works well too.

B. COMPARISON OF ENABLING RESULTS OF IMPROVED ALGORITHM AT DIFFERENT SPEED

To further verify the effectiveness of the improved algorithm, an experimental comparison is made every 10 rpm for the speed from 10rpm to 100rpm, and then the 6th harmonic

amplitude in the error information is obtained by FFT analysis. Subsequently, the comparison chart shown in Fig. 10 is obtained. Fig. 10(a) shows the effect of speed error compensation at different speed and dead time. Fig. 10(b) shows the effect of theta error compensation at different speed and dead time.

C. ANALYSIS OF DYNAMIC TRACKING PERFORMANCE

To verify the dynamic performance of the improved algorithm, Fig. 11 shows the shifting comparison between the traditional algorithm and the improved algorithm in no-load condition. When the conventional position observer is adopted with the initial operation speed at 50rpm, the maximum reachable speed is 250rpm as shown in Fig. 11(a). To achieve a fair comparison, the experimental results using the improved position observer are shown in Fig. 11(b) as well when the motor operates at the same speed changing from 50rpm to 250rpm and then to 50rpm. In Fig. 11, the actual speed θ, estimated speed $\hat{\theta}$, speed error Δn, and position error $\Delta\theta$ are all presented.

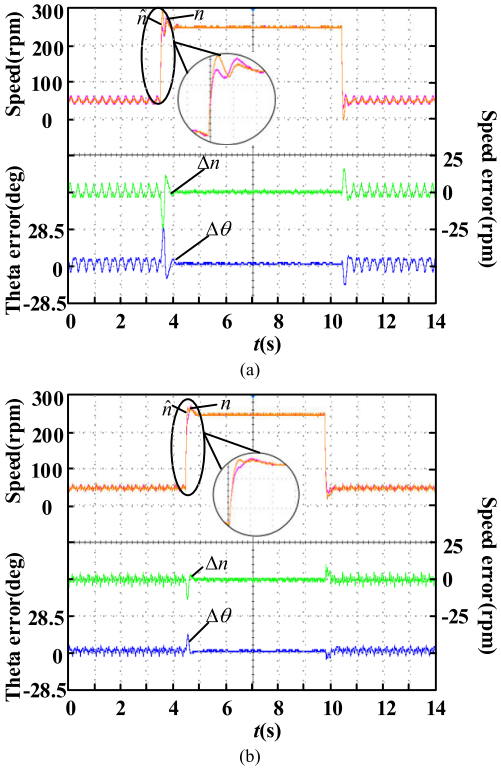

FIGURE 11. The waveform of speed step from 50rpm to 250rpm to 50rpm. (a)conventional position observer. (b)improved position observer.

From Fig. 11, it can be seen that the speed overshoot and response time of the improved position observer are much smaller than those of the traditional observer during the shifting process, and the speed error and position error are reduced a lot. In the traditional position observer, the overshoot of speed error is about 25rpm, and the position error overshoot is about 28.5°. In the improved position observer,

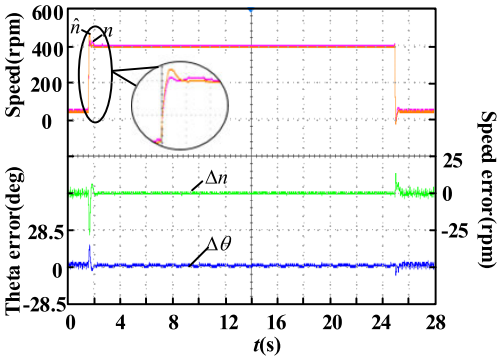

FIGURE 12. The waveform of speed step from 50rpm to 400rpm to 50rpm.

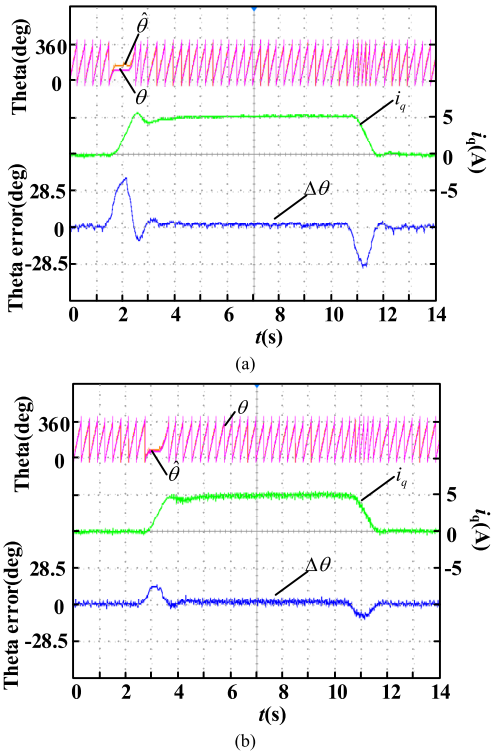

FIGURE 13. The waveform of variable load at 50rpm. (a)conventional position observer. (b)improved position observer.

the overshoot of speed error is about 13rpm, and the position error overshoot is about 14.3°. It is calculated that the speed error overshoot of the improved position observer is 48% lower than that of the conventional observer, and the overshoot of the rotor position error is 49.8%. It can be found that although the estimated rotor position cannot track the actual rotor positon without any difference for the improved position observer because the digital filter still exists in the observer. However, compared with the conventional method, the tracking performance is improved a lot.

As shown in Fig. 12, with the initial operation speed at 50rpm, the maximum reachable speed for the improved position observer is 400rpm. It can be found that the improved algorithm can still run smoothly when the motor is subjected to a wider speed range, indicating that the improved position

observer has good dynamic performance and can operate well under medium speed region.

D. ANALYSIS OF ANTI-DISTURBANCE PERFORMANCE

To verify the anti-disturbance performance of the new algorithm, Fig. 13 shows the load-changing process of the traditional algorithm and the improved algorithm at 50rpm. Fig. 13(a) shows the rotor position, q-axis current and position errors when the conventional algorithm suddenly accumulates 4.4 N·m load. Fig. 13(b) shows the rotor position, q-axis current and position errors when the improved algorithm suddenly accumulates 4.4 N·m load. Fig. 13 exhibits that the improved algorithm can better track the actual rotor position during the process of variable load, and the motor runs more smoothly.

VI. CONCLUSION

In this paper, an improved position observer, which can compensate the position error caused by dead-time effect and improve the dynamic performance of the conventional high frequency signal injection method, is proposed. According to the experimental validation, it can be concluded that compared with conventional pulsating sinusoidal voltage injection method, the improved algorithm can reduce the position estimation error not only in steady state operation conditions, but in variable speed and variable load conditions. And the variable speed range can be widened as well. However, for the proposed observer, there are a lot of parameters, which will bring challenges in selection of the values. Therefore, it should be simplified in the future work.

REFERENCES

[1] X. Zhu, Z. Xiang, L. Quan, W. Wu, and Y. Du, "Multimode optimization design methodology for a flux-controllable stator permanent magnet memory motor considering driving cycles," *IEEE Trans. Ind. Electron.*, vol. 65, no. 7, pp. 5353–5366, Jul. 2018.

[2] G. Wang, Y. Wang, L. Ding, L. Yang, R. Ni, and D. Xu, "Harmonic analysis of the effects of inverter nonlinearity on the offline inductance identification of PMSMs using high frequency signal injection," *J. Power Electron.*, vol. 15, no. 6, pp. 1567–1576, Nov. 2015.

[3] G. Wang, D. Xiao, G. Zhang, C. Li, X. Zhang, and D. Xu, "Sensorless control scheme of IPMSMs using HF orthogonal square-wave voltage injection into a stationary reference frame," *IEEE Trans. Power Electron.*, vol. 34, no. 3, pp. 2573–2584, Mar. 2019.

[4] X. Zhu, Z. Xiang, C. Zhang, L. Quan, Y. Du, and W. Gu, "Co-reduction of torque ripple for outer rotor flux-switching PM motor using systematic multi-level design and control schemes," *IEEE Trans. Ind. Electron.*, vol. 64, no. 2, pp. 1102–1112, Feb. 2017.

[5] C.-H. Hong, J. Lee, and D.-M. Lee, "Sensorless scheme for interior permanent magnet synchronous motors with a wide speed control range," *J. Power Electron.*, vol. 16, no. 6, pp. 2173–2181, Nov. 2016.

[6] G. Zhang, G. Wang, H. Wang, D. Xiao, L. Li, and D. Xu, "Pseudorandom-frequency sinusoidal injection based sensorless IPMSM drives with tolerance for system delays," *IEEE Trans. Power Electron.*, vol. 34, no. 4, pp. 3623–3632, Apr. 2019.

[7] Y. Lee and S.-K. Sul, "Model-based sensorless control of an IPMSM with enhanced robustness against load disturbances based on position and speed estimator using a speed error," *IEEE Trans. Ind. Appl.*, vol. 54, no. 2, pp. 1448–1459, Mar. 2018.

[8] G. Wang, H. Zhou, N. Zhao, C. Li, and D. Xu, "Sensorless control of IPMSM drives using a pseudo-random phase-switching fixed-frequency signal injection scheme," *IEEE Trans. Ind. Electron.*, vol. 65, no. 10, pp. 7660–7671, Oct. 2018.

[9] G. Wang, R. Liu, N. Zhao, D. Ding, and D. Xu, "Enhanced linear ADRC strategy for HF pulse voltage signal injection-based sensorless IPMSM drives," *IEEE Trans. Power Electron.*, vol. 34, no. 1, pp. 514–525, Jan. 2019.

[10] J.-I. Ha, K. Ide, T. Sawa, and S.-K. Sul, "Sensorless rotor position estimation of an interior permanent-magnet motor from initial states," *IEEE Trans. Ind. Appl.*, vol. 39, no. 3, pp. 761–767, May 2003.

[11] Q. Tang, A. Shen, X. Luo, and J. Xu, "PMSM sensorless control by injecting HF pulsating carrier signal into ABC frame," *IEEE Trans. Power Electron.*, vol. 32, no. 5, pp. 3767–3776, May 2017.

[12] J. M. Wang and J. W. Gao, "Influence of speed EMF on position estimation error in carrier signal injection based sensorless control of PMSM," in *Proc. ICEM*, Oct. 2012, pp. 1–6.

[13] L. Ying, Z. Bo, F. Ying, W. Jiadan, and S. Mingming, "Sensorless control with two types of pulsating high frequency signal injection methods for SPMSM at low speed," in *Proc. 4th Int. Conf. Power Electron. Syst. Appl.*, Jun. 2011, pp. 1–5.

[14] D. Raca, P. Garcia, D. Reigosa, F. Briz, and R. Lorenz, "A comparative analysis of pulsating vs. Rotating vector carrier signal injection-based sensorless control," in *Proc. 23rd Annu. IEEE Appl. Power Electron. Conf. Expo.*, Feb. 2008, pp. 879–885.

[15] G. Zhang, G. Wang, B. Yuan, R. Liu, and D. Xu, "Active disturbance rejection control strategy for signal injection-based sensorless IPMSM drives," *IEEE Trans. Transport. Electrific.*, vol. 4, no. 1, pp. 330–339, Mar. 2018.

[16] A. T. Woldegiorgis, X. Ge, S. Li, and M. Hassan, "Extended sliding mode disturbance observer-based sensorless control of IPMSM for medium and high-speed range considering railway application," *IEEE Access*, vol. 7, pp. 175302–175312, Dec. 2019.

[17] R. Raute, C. Caruana, C. S. Staines, J. Cilia, M. Sumner, and G. M. Asher, "Analysis and compensation of inverter nonlinearity effect on a sensorless PMSM drive at very low and zero speed operation," *IEEE Trans. Ind. Electron.*, vol. 57, no. 12, pp. 4065–4074, Dec. 2010.

[18] Z. Zhang, H. Guo, Y. Liu, Q. Zhang, P. Zhu, and R. Iqbal, "An improved sensorless control strategy of ship IPMSM at full speed range," *IEEE Access*, vol. 7, pp. 178652–178661, Dec. 2019.

[19] Y.-D. Yoon, S.-K. Sul, S. Morimoto, and K. Ide, "High-bandwidth sensorless algorithm for AC machines based on square-wave-type voltage injection," *IEEE Trans. Ind. Appl.*, vol. 47, no. 3, pp. 1361–1370, May 2011.

[20] N.-C. Park and S.-H. Kim, "Simple sensorless algorithm for interior permanent magnet synchronous motors based on high-frequency voltage injection method," *IET Electr. Power Appl.*, vol. 8, no. 2, pp. 68–75, Feb. 2014.

[21] P. L. Xu and Z. Q. Zhu, "Carrier signal injection-based sensorless control for permanent-magnet synchronous machine drives considering machine parameter asymmetry," *IEEE Trans. Ind. Electron.*, vol. 63, no. 5, pp. 2813–2824, May 2016.

[22] M. Seilmeier, S. Ebersberger, and B. Piepenbreier, "PMSM model for sensorless control considering saturation induced secondary saliencies," in *Proc. IEEE Int. Symp. Sensorless Control Electr. Drives Predictive Control Electr. Drives Power Electron. (SLED/PRECEDE)*, Oct. 2013, pp. 1–8.

[23] S.-H. Hwang and J.-M. Kim, "Dead time compensation method for voltage-fed PWM inverter," *IEEE Trans. Energy Convers.*, vol. 25, no. 1, pp. 1–10, Mar. 2010.

[24] B. Liu, B. Zhou, and T. H. Ni, "Inverter nonlinearity compensation for SPMSM sensor-less control based on second-order generalized integrator," *Proc. CSEE.*, vol. 38, no. 11, pp. 3365–3374 Jun. 2018.

[25] Z. Zhou, C. Xia, Y. Yan, Z. Wang, and T. Shi, "Disturbances attenuation of permanent magnet synchronous motor drives using cascaded predictive-integral-resonant controllers," *IEEE Trans. Power Electron.*, vol. 33, no. 2, pp. 1514–1527, Feb. 2018.

[26] J. He, Y. Wei Li, F. Blaabjerg, and X. Wang, "Active harmonic filtering using current-controlled, grid-connected DG units with closed-loop power control," *IEEE Trans. Power Electron.*, vol. 29, no. 2, pp. 642–653, Feb. 2014.

[27] Z. Pan, F. Dong, J. Zhao, L. Wang, H. Wang, and Y. Feng, "Combined resonant controller and two-degree-of-freedom PID controller for PMSLM current harmonics suppression," *IEEE Trans. Ind. Electron.*, vol. 65, no. 9, pp. 7558–7568, Sep. 2018.

[28] M. Ramezani and O. Ojo, "The modeling and position-sensorless estimation technique for a nine-phase interior permanent-magnet machine using high-frequency injections," *IEEE Trans. Ind. Appl.*, vol. 52, no. 2, pp. 1555–1565, Apr. 2016.

YI MAO received the B.S. degree in automation from the Luoyang Institute of Science and Technology, Luoyang, China, in 2017. He is currently pursuing the Ph.D. degree in electrical engineering with Jiangsu University, Zhenjiang, China.

His research interests include motor design and sensorless control of PM motor.

YI DU (Member, IEEE) received the B.Sc. and M.Sc. degrees in electrical engineering from Jiangsu University, Zhenjiang, China, in 2002 and 2007, respectively, and the Ph.D. degree in electrical engineering from Southeast University , Nanjing, China, in 2014.

He has been with Jiangsu University since 2002, where he is currently an Associate Professor with the School of Electrical and Information Engineering. His research interests include design and analyze electric machine system with low-speed and high-torque output and wide-speed range.

ZHUOFAN HE received the B.Sc. degree from Jiangsu University, Zhenjiang, China, in 2019. He is currently pursuing the master's degree in electrical engineering with Jiangsu University, Zhengjiang, China. His current research interest includes electric machine design.

LI QUAN received the B.Sc. degree in electric machines and electric apparatus from the Hefei University of Technology, Hefei, China, in 1985, the M.Sc. degree in electric machines and electric apparatus from Southeast University, Nanjing, China, in 1991, and the Ph.D. degree in power electronics and power transmission from the Nanjing University of Aeronautics and Astronautics, Jiangsu, China, in 2007.

Since 1998, he has been with Jiangsu University, Zhenjiang, China, where he is currently a Professor with the School of Electrical and Information Engineering. He has authored or coauthored more than 100 technical articles and one textbook. He holds three patents in these areas. His teaching and research interests include high-performance permanent magnet motors for electric vehicles, double rotor permanent-magnet motors for hybrid electric vehicles, and motor drive control.

XIAOYONG ZHU (Member, IEEE) received the B.Sc. and M.Sc. degrees in electrical engineering from Jiangsu University, Zhenjiang, China, in 1997 and 2002, respectively, and the Ph.D. degree in electrical engineering from the School of Electrical Engineering, Southeast University, Nanjing, China, in 2008.

He has been with Jiangsu University since 1997, where he is currently a Professor with the School of Electrical Information Engineering. From 2007 to 2008, he was a Research Assistant with the Department of Electrical and Electronic Engineering, The University of Hong Kong. From 2012 to 2013, he was a Visiting Professor with the Graduate Automotive Technology Education Center for Electric Drive Transportation, funded by the Department of Energy, University of Michigan, Dearborn, MI, USA. His current research interests include design and drive control of electric machines with wide-speed range, less rare-earth permanent-magnet motors, and multiport permanent-magnet motors.

LI ZHANG (Member, IEEE) received the B.Sc. degree in electrical engineering and automation from Jiangsu University, Zhenjiang, China, in 2010, and the M.Sc. and Ph.D. degrees in electrical engineering from Southeast University, Nanjing, China, in 2013 and 2018, respectively.

From February 2016 to February 2017, she was a Joint Ph.D. Student with WEMPEC, University of Wisconsin-Madison, Madison, WI, USA. She is currently a Lecturer with the School of Electrical and Information Engineering, Jiangsu University. Her research interests include electric machines and drives.

YUEFEI ZUO (Member, IEEE) received the B.Sc. and Ph.D. degrees in electrical engineering and automation from the Nanjing University of Aeronautics and Astronautics, Nanjing, China, in 2010 and 2016, respectively. He has been a Lecturer with Jiangsu University, since July 2016. He is currently a Postdoctoral Research Fellow with the School of Electrical and Electronic Engineering, Nanyang Technological University, Singapore. His research interest includes advanced control strategies for high-performance electric drives.